ORIGINAL RESEARCH ARTICLE

AISI 316L Stainless Steel Tribological Behavior under Sliding and Erosive Conditions: A Comparison between Spark Plasma Sintering, Laser Metal Deposition, and Cold Spraying

A.V. Radhamani, Hon Chung Lau, Anirudh Venkatraman Krishnan, M. Kamaraj, and S. Ramakrishna

Differently processed AISI 316L SS samples were studied to understand the impact of the fabrication process on their tribological and erosion behavior. Samples processed by spark plasma sintering (SPS), laser metal deposition (LMD), and cold spraying (CS) were compared with a commercial grade steel sample. Tribotests were performed at 28 °C and 500 °C using a ball-on-disk tribometer under a normal load of 10 N at dry sliding conditions. Parameters such as hardness, bond strength, and secondary phases show major roles in deciding the wear resistance of a material. Tribotests revealed that the cold sprayed sample has the highest wear rate of $\sim 1.4 \times 10^{-4}$ mm^3/N m at 28 °C and the lowest wear rate of $\sim 0.22 \times 10^{-4}$ mm^3/N m at 500 °C. At 28 °C, the SPS and commercial grade steel samples showed nearly the same wear rate of $\sim 0.40 \times 10^{-4}$ mm^3/N m while LMD showed a wear rate of $\sim 0.66 \times 10^{-4}$ mm^3/N m. At 500 °C, SPS, LMD, and commercial grade 316 LSS showed a wear loss of ~ 0.56, ~ 0.32, and $\sim 0.66 \times 10^{-4}$ mm^3/N m, respectively. Erosion is a serious issue in many applications and is addressed in our study to understand the suitability of fabricated samples under erosive conditions. Erosion studies were carried out using an air–sand erosion tester at two different blasting angles, namely, 45° and 90°. The highest erosion rate was observed in the CS sample which might be due to the weaker bonding between the as-sprayed particles.

A.V. Radhamani, Energy and Innovative Materials Laboratory (EIML), Department Physics and Nanotechnology, SRM Institute of Science and Technology, Kattankulathur, Chennai 603 203, India; **Hon Chung Lau**, Department of Civil and Environmental Engineering, National University of Singapore, Singapore 119260, Singapore; **Anirudh Venkatraman Krishnan**, Department of Mechanical Engineering, Sri Sivasubramaniya Nadar College of Engineering, Kalavakkam, Chennai 603110, India; **M. Kamaraj**, Department of Metallurgical and Materials Engineering, Indian Institute of Technology Madras, Tamilnadu 600036, India; and and **S. Ramakrishna**, Department of Mechanical Engineering, Centre for Nanofibers and Nanotechnology, National University of Singapore, Singapore 119260, Singapore. Contact e-mail: radhamaa@srmist.edu.in.

Graphical Abstract
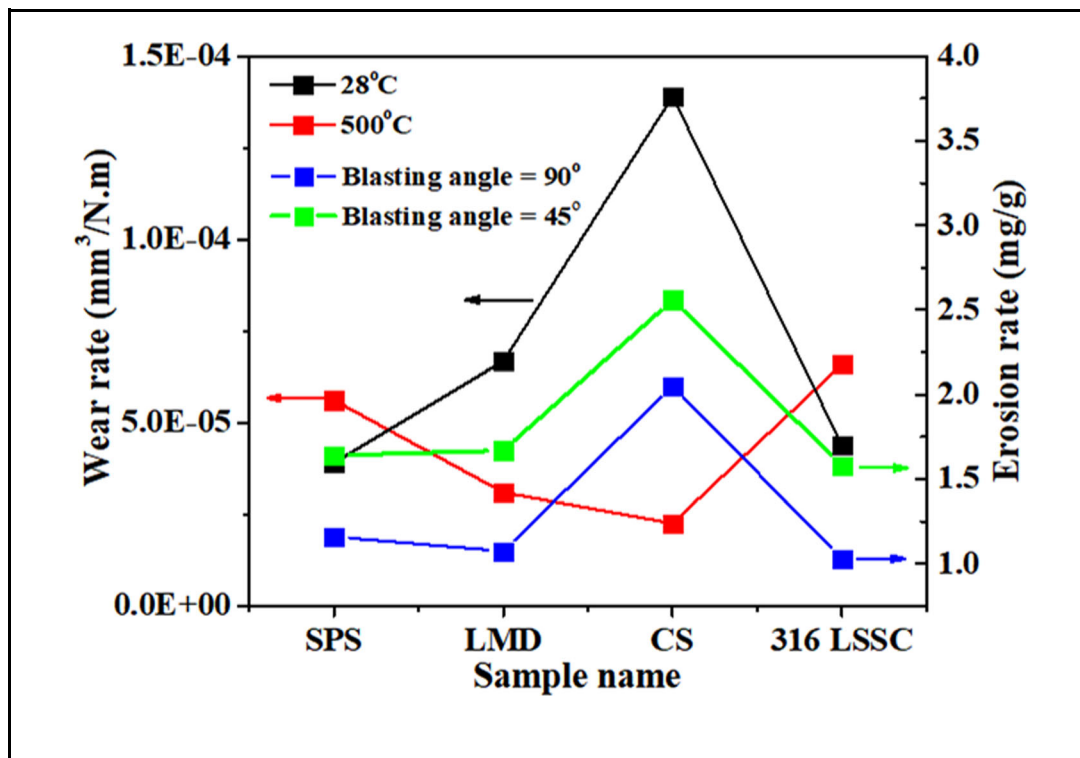
1. Introduction

Austenitic stainless steel (SS) has applications in numerous fields due to its strength, toughness, weldability, ductility, durability, and low production cost (Ref 1). 316 LSS stands out among various grades due to its high corrosion resistance and weldability. There are many ways to process metals, alloys, and composites depending on the applications. Traditional casting to brand new spark plasma sintering (SPS) processes is used in powder metallurgy for the various materials processing (Ref 2). Additive manufacturing (AM) is gaining attention in recent years for making 3D structure of many materials starting from polymer to metals/metal composites (Ref 3). Samples for the present study were prepared by spark plasma sintering (SPS) and AM techniques such as laser melt deposition (LMD) and cold spraying (CS) (Fig. 1). In the SPS process, short sintering time and low sintering temperature are favorable for consolidating the powder without considerable grain growth (Ref 4). The LMD has a very high deposition rate (3-5 kg/h) and uses a laser to melt the powder which is injected on to the substrate. In CS, solid powders are accelerated to high speed of ∼ 1200 m/s onto a substrate where they undergo plastic deformation and adhere to the surface (Ref 5, 6). Three processing methods (SPS, LMD, and cold spray) were chosen due to their advantages over other processes and the availability of instruments within our grasp. Processing methods can have a

direct impact on the structural, mechanical, and tribological behavior of steel (Ref 7).

Many studies have been conducted on the processing and characterization of various structural, microstructural, and mechanical properties of 316 SS and other graded steel at both ambient and high temperatures (Ref 8–11). However, studies on the tribological properties of 316 SS produced under different processes and conditions are scarce though they are very crucial for industrial application. Alvi et al. (Ref 12) studied the tribological properties of selective laser melted (SLM) 316 SS at room and high temperatures. They observed that the wear rates at 300 °C and 400 °C are twofold lower than the corresponding room temperature values and attributed the change to the stable microstructure, cellular grains, oxide glaze formation, and hardness. Bartolomeu et al. (Ref 13) compared the tribological performance of hot pressed 316 LSS, SLM, and casted steel in a lubricant solution (phosphate-buffered saline (PBS)). Dense steel can give high wear resistance compared to less dense steel as revealed in the studies of Sun and group (Ref 14). Tribological properties of SLM processed 316 LSS were studied by Zhu et al. (Ref 15) under lubricating conditions. They observed improved wear and friction values compared to the traditionally processed steel due to pores and refined grains present in the SLM processed sample. SLM deposited metal/alloy samples are widely used in tribological studies than other processed samples as they are the most widely used material in SLM. Hence, the present study helps to identify the knowledge gap in the literature.

Erosion is a major problem in many industrial applications such as oil and gas catalytic cracking, hydraulic and gas turbines, coal turbines, and sand blasting. There are many reports on the erosion aspects of various grades of steel. For example, SUS 304SS was studied by Nguyen (Ref 16) for its
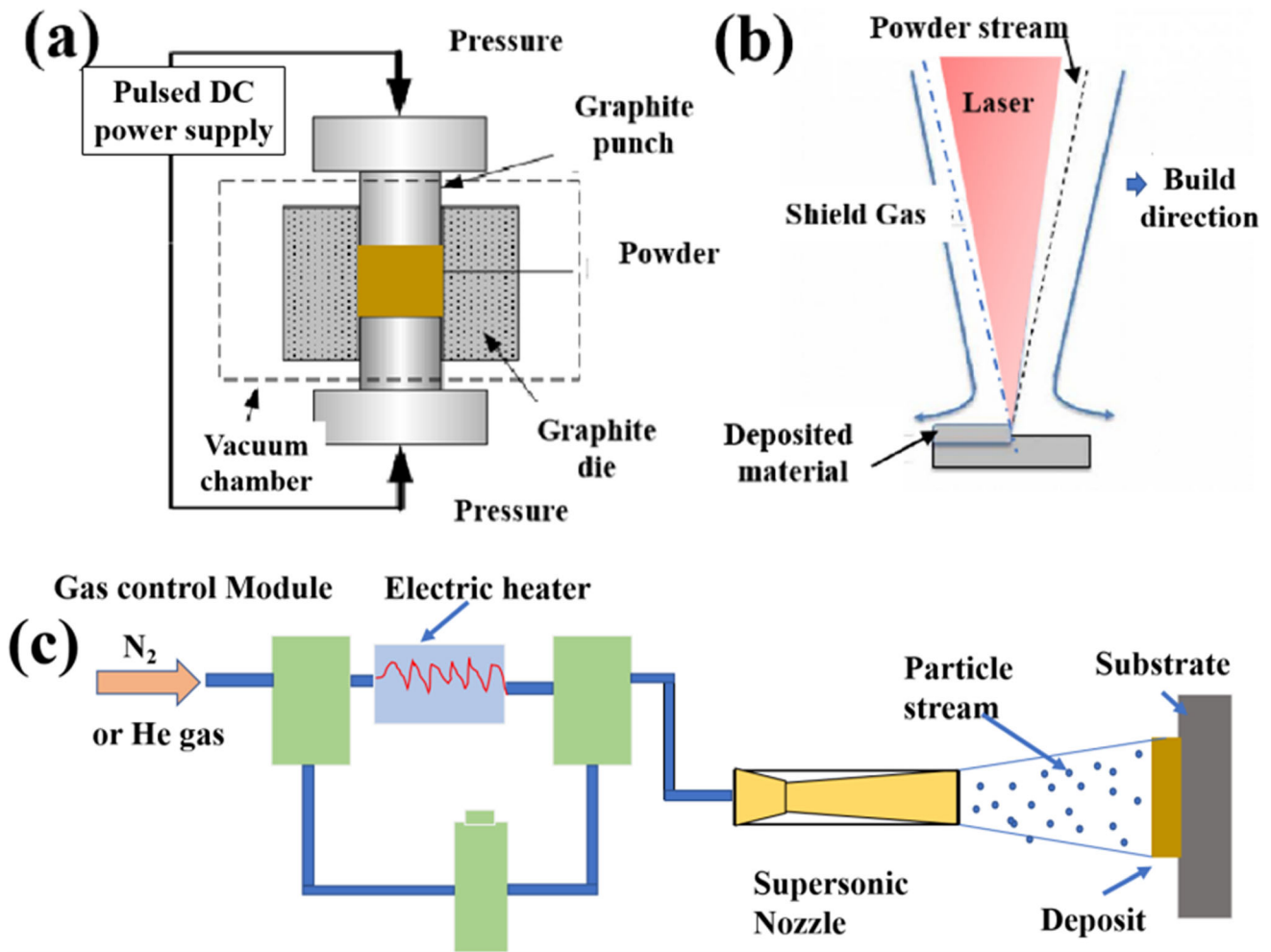
Fig. 1 Schematic of fabrication processes (a) spark plasma sintering, (b) laser metal deposition, and (c) cold spray

erosion rate and mechanism both experimentally and theoretically. For the erosion resulting from a particle stream, stream characteristics of the particles were found to play a vital role (Ref 17, 18). Nguyen and group explored the effect of erodent particle size on the erosive behavior (Ref 19). They calculated the erosion as a function of impinging angle, sand particle flux, and impinging velocity. There are many parameters which determine the erosion resistance, yet microstructure plays an important role. Aniruddha et al. (Ref 20) investigated the role of carbides on the erosion resistance of nitronic steel. Their studies showed that the carbides present in the 23-8-N steel reduce the erosion resistance as they cause cracking and matrix decohesion. The morphology, volume, and the distribution of carbides also influence the erosion rate. However, only few studies were reported on the erosion resistance of 316 SS. Wood et al. (Ref 21) examined the evolution of surface microstructure when 316 SS was subjected to both erosion and erosion–corrosion process by using focused ion beam (FIB) and transmission electron microscopy (TEM) techniques. It was observed that solid particle erosion caused extensive crater and lip formations and a martensitic phase transformation at the surface. In the presence of corrosive fluid, authors observed the dissolution of martensitic phase followed by reduction in work hardening behavior and hence resulted at higher erosion–corrosion rates. Erosion of 316 SS was compared to those of

304 SS and 420 SS grades by Laguna-Camacho et al. (Ref 22). They found that AISI 304 and 316 SS gave rise to similar erosion resistance while AISI 420 gave the best erosion resistance at all tested angles. The difference in the erosion resistance was attributed to the ductile (AISI 420) and brittle nature (AISI 304 and 420 SS) of the different steel grades. The low erosion resistance of austenitic stainless steel can be further improved by the application of metallic or ceramic coatings (Ref 23-25).

The operating parameters selection for sliding and erosion tests are based on the literature survey and some of the real-world cases. For example, selection of impact angle as 45° and 90° is to understand both the maximum and minimum erosive behaviors of the differently processed samples. At all other impact angles, erosion rates lie between the maximum and minimum values. Moreover, the main objective of the studies was to compare the erosion and sliding behavior of differently processed steels. Hence, we have done few essential studies within the scope of this manuscript. The objective of the present study is to understand the tribological behavior under sliding and erosive conditions for differently processed 316 LSS samples. Results reveal the effect of fabrication process on material properties which can give insights into the choice of fabrication methods for specific applications.

2. Materials and Characterization

2.1 Materials and Processing

Samples were processed by spark plasma sintering (SPS), laser metal deposition (LMD), and cold spray (CS) techniques, and detailed processing conditions including the comparison of microstructure, mechanical, and corrosion properties were reported elsewhere (Ref 26). The properties of the processed blocks of stainless steel are further compared to those of commercially available casted grade. Stainless steel carbon grade AISI 316L with an average particle size of 45 μm was used as a powder starting material for the fabrication process. Powders were used as received without any further purification. The SPS was done at a sintering temperature of 1000 °C at a heating rate of 50 °C/min while LMD process involved a temperature of 1800 °C and a feeding rate of 8 g/min. In the cold spray, feed rate was set as 30 g/min, and the powders experienced a low temperature of $\sim$ 400 °C (gas heating temperature).

2.2 Characterization

For the sliding and erosion tests, all the samples were cut in square shapes with a dimension of 2 cm x 2 cm and polished using grit papers whose particle sizes were ranging from 18 to 1 μm. Vicker's hardness was carried out using 'HMV Shimadzu' tester. Hardness was done using an indentation load of 0.5 kg at a holding time of 15 s. The compressive properties of the samples were tested using an automated hydraulic testing machine (MTS 810). A strain rate of 0.06 mm/s was used for all the samples. Cylindrical pellets (6-mm diameter and 6-mm length) were used for the tests. A ball-on-disk tribometer (Nanovea, USA) was used to measure the friction and wear characteristics of differently processed 316 LSS. All the measurements were done at room temperature in atmospheric pressure without using any lubricant. The normal load, sliding distance, and rotation speed used for the tests were 10 N, 500 m, and 500 rpm, respectively. For all samples, the wear track diameter was set as 4 mm. The samples were cut in a square shape with a dimension of 2 cm $\times$ 2 cm and polished using grit papers whose particle sizes were ranging from 18 to 1 μm. A Zirconia ball ($\sim$ 3-mm diameter) with a hardness value of $\sim$ 1200 HV was used as the counter body. For each sample, three tests were conducted to confirm the reproducibility. The zirconia ball is stationary and in contact with the sample disk which is rotating at a given speed. Zirconia is an excellent material for use in tribotests against soft materials due to its overall high hardness, high-temperature resistance, low friction coefficient, and chemical resistance. A high-resolution scanning electron microscope (HRSEM-JEOL) equipped with an energy-dispersive x-ray spectroscopy (EDXS) was used to image the wear track and elemental composition of tribo-tested sample. The size and shape of the erodent and grain structure of all the differently processed samples were analyzed by an optical Leica microscope. A three-dimensional view of the worn and eroded surface was recorded using a 3D surface profiler (AEP Technology, Nano Map). The wear and erosion scar depth profiles were further deduced from 3D profiles. The wear rate was calculated by measuring the wear volume obtained from the 2D profile (Ref 2), and erosion rate from the weight loss and quantity of erodent used. Erosion behavior was studied using an air–sand erosion tester (PANBLAST PB250P) equipped with

an air compressor of capacity $\sim$ 12 bar. To make sure the air supply to the tester was clean and dry, the tester was incorporated with a dryer and air filter. The air flow in the tester was controlled by a pressure regulator. All studies were conducted using alumina (Al_2O_3) particles of average particle size 150 μm. Each sample with a dimension of 20 mm (l) $\times$ 20 mm (b) $\times$ 5 mm (t) was exposed to continuous blasting for one minute. Experiments were repeated three times for each sample to calculate the possible system fluctuations. The sample holder was set at a distance of 25 mm away from the blast nozzle ($\sim$ 9-mm diameter and $\sim$ 45-mm length). Air–sand was accelerated through a 1-m long steel tube before hitting the surface of sample. The blasting angle could be adjusted from 0 to 90° by rotating the sample holder. In the our experiments, two blasting angles, viz, 90° and 45°, were selected. The sand hopper has a capacity to carry $\sim$ 10 kg of sands and has auto-pressure feedback to control the sand flow rate. We have used 120 g of sand for each experiment.

In the results and discussion part, stainless steel is abbreviated as 'SS,' AISI 316 low carbon stainless steel as '316 LSS,' and 316L commercial grade stainless steel as '316 LSSC.'

3. Results and Discussion

3.1 Microstructures and Mechanical Properties

Microstructural and mechanical studies were carried out on all the samples mentioned in the present work, and the results had published in our previous work (Ref 26). Major observations are summarized briefly here for the readers reference. Figure 2(a–d) shows the morphological structure of the prepared samples. The grain size of the SPS and 316 LSSC samples is comparable and of the order of 20 μm. Cellular grains with average size of 0.3 μm are seen in LMD samples while the CS samples showed a larger austenitic grains of average size $\sim$ 36 μm.

Hardness and compressive strength of the samples are tabulated in Table 1 and shown below. Hardness and compression test studies showed that cold sprayed sample has highest hardness and compressive strength compared to other samples. Cold sprayed sample showed the highest hardness (378 HV) compared to the other samples, viz, SPS (244 HV), LMD (258 HV), and 316 LSSC (226 HV). The compressive yield strength of SPS, LMD, CS, and 316 LSSC samples was found to be 501, 639, 1391, and 800 MPa, respectively.

As can be seen from the optical images, different processes yielded different kinds of grains and hence showed variation in their mechanical properties. Hardness of a sample is decided by many parameters such as grain size, particle–particle bond strength, density, and presence/nature of secondary phases. As per the Hall–Petch relation, grain size and hardness or compressive strength are inversely related (Ref 27). The CS sample showed that the highest hardness though the average grain size is larger. This hardness behavior can be correlated to the resistance of the sample to the plastic deformation (Ref 28). Compressive test gives the information about the bulk property of the material unlike the surface information by hardness test. Grain size reduction and secondary phase formation can help in enhancing the resistance to the plastic deformation. Nevertheless, in CS sample, higher yield strength is observed due to the inherent nature of high resistance of the sample to the plastic
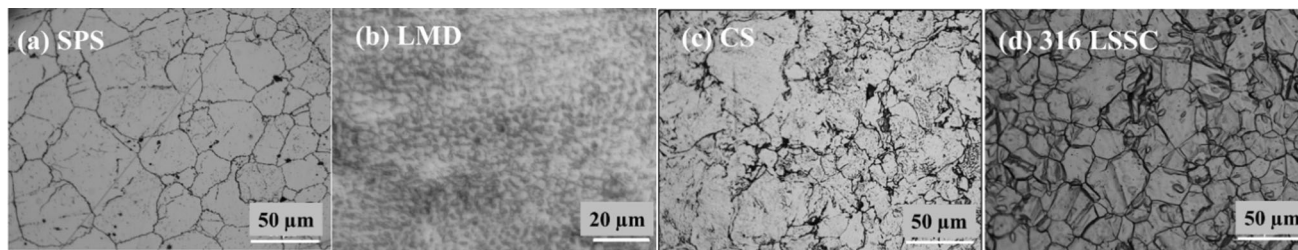
Fig. 2 Optical images of (a) SPS, (b) LMD, (c) CS, and (d) 316 LSSC samples. Reproduced from Ref 26 with permission

Table 1 The hardness and compressive yield strength values of SPS, LMD, CS, and 316 LSSC samples

Sample ID	Hardness, HV	Compressive yield strength, MPa
SPS	244 ± 5	501 ± 20
LMD	258 ± 5	639 ± 20
CS	378 ± 5	1391 ± 20
316 LSSC	226 ± 5	800 ± 20

deformation. The presence of carbide secondary phase helped in getting high yield strength for 316 LSSC. In general, grains and impurity phases serve as pinning points for dislocations movement and delay the onset of plastic deformation (Ref 29).

The application of a material is decided by its specific properties which is further decided by the process methods. As an example, cold sprayed sample can be used for applications that need higher hardness and yield strength. Exploration of tribological properties helps in determining the other applications of differently processed steels.

3.2 Tribological Studies

All the differently processed samples along with casted commercial grade sample were tested for tribological behavior at both room and a high temperature (500 °C). Low wear rate materials can find potential applications where a high wear resistant steel is required. Tests at the high temperature were conducted to understand the possible high-temperature applications of SS structures. As opposed to room temperature, high temperatures have the following issues related to tribology: *(i) Increased wear:* Increased wear can be expected given the higher thermal energy and the material's propensity to soften and deform. This may lead to shorter component lives and higher maintenance costs. *(ii) Elevated friction*: Materials tendency to adhere to one another at high temperatures can increase friction and heat production. This may result in a component seizure or failure. *(iii) Oxidation and corrosion*: High temperatures can cause oxidation and corrosion of materials, especially when there is air or other reactive gases present. Surface deterioration and performance degradation may result from this. *(iv) Reduced lubrication effectiveness*: High temperatures can cause lubricants to break down or evaporate, which increases wear and friction while decreasing lubrication effectiveness. *(v) Thermal expansion*: Expanding materials at high temperatures can affect the geometry of components and raise stresses that can lead to failure. Overall, high-temperature tribology is a complicated topic that neces-

sitates careful consideration of material selection, lubrication, and operating conditions in order to minimize wear, reduce friction, and guarantee the consistent performance of components. Here, high-temperature analysis to comprehend wear and friction for variously processed AIS316L stainless steel was taken into consideration.

3.2.1 Room Temperature (28 °C) Test

(i) Friction

Variations in the frictional values with respect to the sliding distance for SPS, LMD, CS, and 316 LSSC samples are shown in Fig. 3(a) with the corresponding average friction coefficient in Fig. 3(b).

As can be seen from the plots that the SPS sample showed nearly constant coefficient of friction (COF) after a sliding distance of ∼ 100 m. The rest of the samples revealed large fluctuation in friction coefficient while commercial grade showed a maximum from 0.50 to 0.65 after a sliding distance of 280 m. Cold spray was found to show less fluctuation compared to the laser melt sample. Based on average friction values, cold spray showed lowest value (0.43) while 316 LSSC highest value (0.56). The SPS and LMD samples had the same friction coefficient value (0.47). Fluctuations can be attributed to the non-conformal to conformal contact between the mating surfaces, stiffness, and hardness difference between the samples. The zig–zag nature of frictional curves further indicates the irregular wear rate. In the present case, the harder the material, the lower is the frictional coefficient, if other parameters are constant. In softer materials, the relative motion between the surfaces will be prevented as the material easily undergo fracturing. Although hardness has little effect on friction, there is evidence that in general, the friction is less with harder metals. For example, experiments on a carefully selected series of copper–beryllium alloys show that the friction decreases linearly with the hardness (Ref 30). Also, it had shown that lower friction coefficient in harder material is due to stronger inter-atomic linking bonds (Ref 31).

Two materials possessing the same friction coefficient do not mean that they have the same wear rate. As a consequence of the mating between surfaces, there will be energy transfer which can either be stored in the material or dissipated in a number of ways. The mechanical energy resulted from sliding could be converted into different ways such as heat, vibrations, fracturing/new surface formation, defect formation, and plastic deformation. Hence, the partition of total energy resulting from the sliding contact into the energy stored in the system and energy dissipated to the surrounding will be different for different materials (Ref 32).
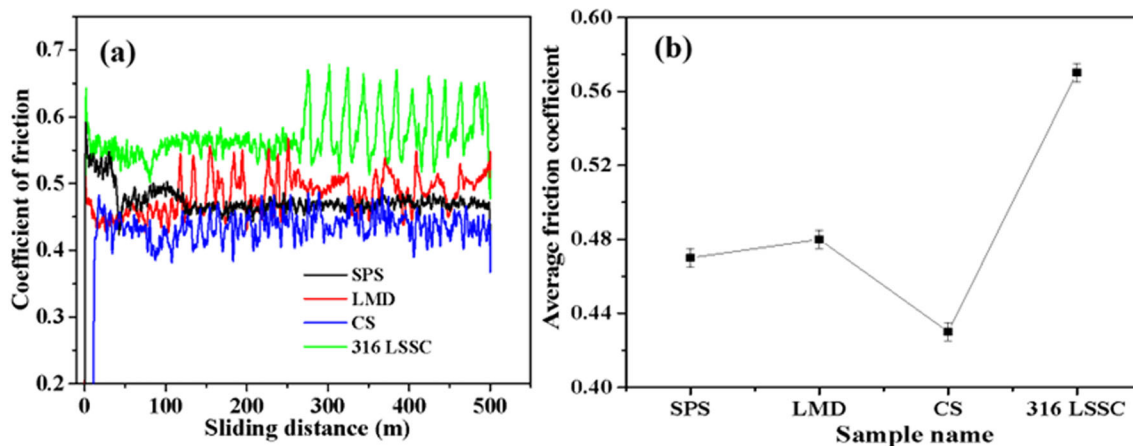
Fig. 3 (a) Coefficient of friction against sliding distance and (b) average friction coefficient for differently processed samples

(ii) Wear

To understand more about the wear rate qualitatively and quantitatively, 3D profiles of the tribo-tracks were recorded and shown in Fig. 4. It can be seen that the cold spray sample has the highest crater depth and width. The SPS and commercial grade appear to give almost same wear craters, while LMD shows a slightly higher wear track width.

To confirm and quantify the observations made from the 3D imaging, two-dimensional depth profiles were extracted and shown in Fig. 5(a). Track depth and track width for the CS sample showed highest values of 87.3 μm and 1349 μm, respectively, as compared to the other samples. The SPS and commercial samples gave almost similar and lowest values for width and depth. The wear volume estimated for SPS, LMD, CS, and 316 LSSC are 0.0.20, 0.33, 0.70, and 0.22 mm^3, respectively. The wear rate is more conveniently used to represent the wear resistance of a material. The wear rate was calculated for all the samples from the track depth and track width, and the same is plotted in Fig. 5(b). Though the hardness and yield strength of cold spray sample are highest compared to other samples, its wear rate (1.4 $\times$ 10^{-4} mm^3/N.m) is about 3.5 times more than that of SPS sample.

The hardness of SPS, LMD, CS, and 316 LSSC was 245, 257, 378, and 226 HV, respectively, at 0.5 kg. The corresponding yield strength was 501, 640, 1391, and 805 MPa, respectively. The highest wear volume in case of cold sprayed sample despite the above values can be explained as follows. The microstructural studies on the CS sample reveal that the deposited particles are intensely deformed, and the average particle size is of the order of 36 μm (Fig. 2c), and particles are found in elongated shapes. The deformation was found to be higher at the interparticle boundaries. Many studies on microstructure of the cold sprayed metallic particles unraveled clear particle boundaries *via* etching. They show that the deposited particles are not strongly bonded (Ref 33). The intense plastic deformation resulted in a higher value for hardness and yield strength. The ultimate compressive strain

values found for cold spray sample are 63% strain while 68% for LMD and 69.7% SPS. The 316 LSSC showed no failure until confronted with 80% of strain and was more ductile in nature. All samples except the commercial grade could withstand similar stress $\sim$ 3600 MPa but had undergone different levels of strain. The CS sample failed under compression before other samples. In general, cold sprayed samples would be annealed at different temperatures for re-crystallization and grain growth (Ref 34). Mccune et al. (Ref 35) confirmed that elongated grains at the interface recrystallized and grain sizes matched that of the starting powder. The effect of annealing is evident from the high-temperature tribotest.

The SPS and 316 LSSC samples showed nearly same wear rate (4 $\times$ 10^{-5} mm^3/N m) which is in good agreement with their comparable grain size (20 μm). LMD sample showed slightly higher wear rate (6.3 $\times$ 10^{-5} mm^3/N m) compared to the SPS and 316 LSSC samples. Fine grains ($\sim$ 0.3 μm) of LMD samples were expected to give lower wear rate. However, the parameters such as surface roughness, porosity, and residual stress in the samples can enhance the wear rate.

The FESEM images of the worn surfaces of the room temperature tested samples were taken and shown in Fig. 6. The wearing out of a material mainly depends on the nature of the material, operating conditions, and contact mode. In general, cracking, delamination, and tearing out can be seen in all the samples as evidenced form the surface morphology. In all the cases, as the rubbing of the matting surfaces caused small chips or particles to break off, abrasive wear is the predominant wear mechanism. From the HRSEM images, the possible wear mechanism in a zirconia steel matting body can be summarized as (i) *Abrasive wear*: As harder particles of zirconia rub against the steel, causing material to be removed from both the surfaces, and (ii) *Adhesive wear*: In the present case, close contact of the surfaces for a longer period and the insufficient lubrication can cause the adhesive wear. The particles or debris available in the contact region as seen in the images can enhance the abrasive war.
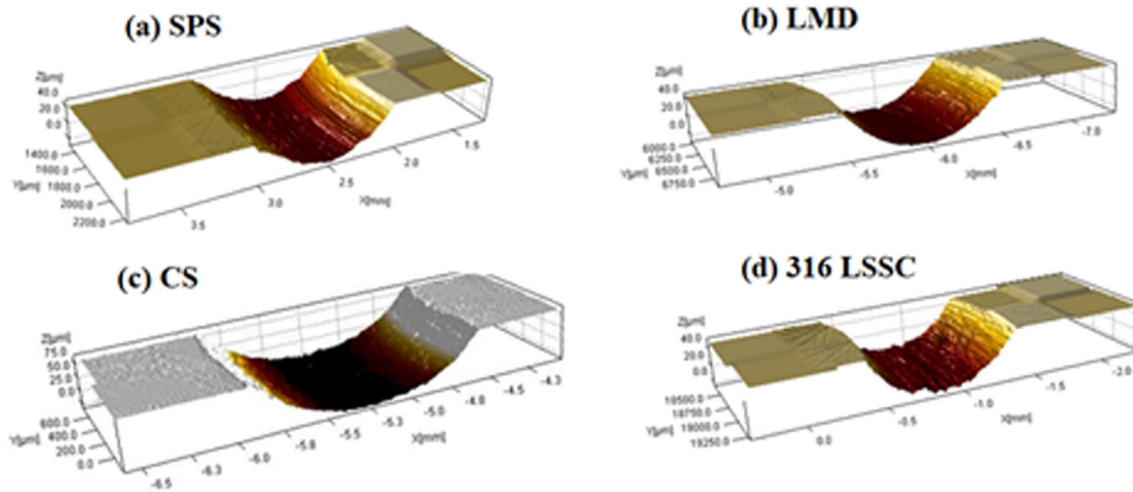
Fig. 4 Three-dimensional optical profile images of the wear track of the room temperature tested samples (a) SPS, (b) LMD, (c) CS, and (d) 316 LSSC
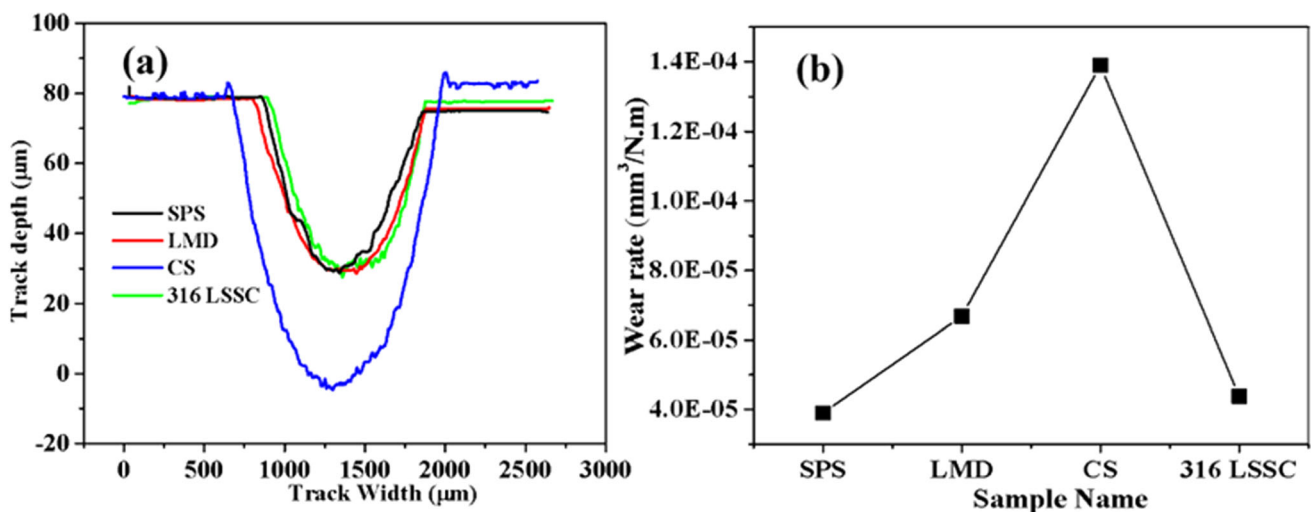

Fig. 5 (a) Two-dimensional depth profiles and (b) wear loss volume of differently processed samples and commercial grade casted steel
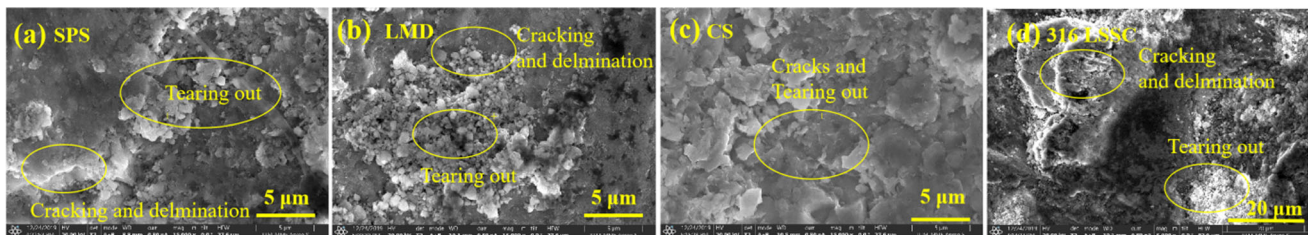

Fig. 6 Morphology of samples after the room temperature wear test ; (a) SPS, (b) LMD, (c) CS, and (d) 316 LSSC

3.2.2 High-Temperature (500 °C) Test

(i) Friction

The frictional behavior obtained from the high-temperature test is plotted in Fig. 7(a). In all the samples, we can see an initial running-in stage with an increase in the coefficient of friction (COF) during the first 50-m distance. Nearly constant COF values were seen for SPS, LMD, and CS samples after a sliding distance of 200 m. The values of average COF are plotted in Fig. 7(b). All samples showed nearly same average COF values except for the commercial grade. The high-temperature COF for 316 LSSC was reduced significantly after a sliding distance of 200 m compared to the remaining samples and its corresponding room temperature value.
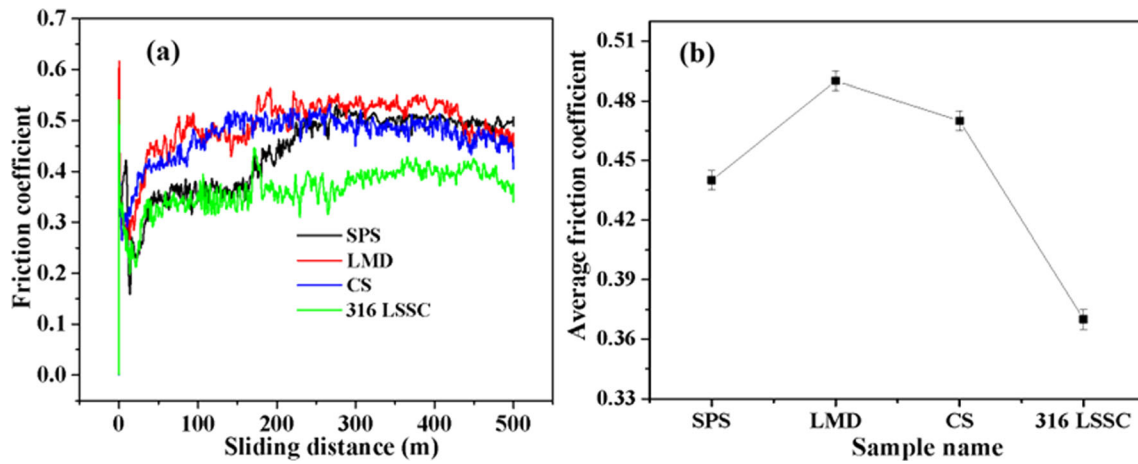
Fig. 7 (a) Variation of coefficient of friction as a function of sliding distance and (b) average friction coefficient for all the samples during high-temperature tribotest
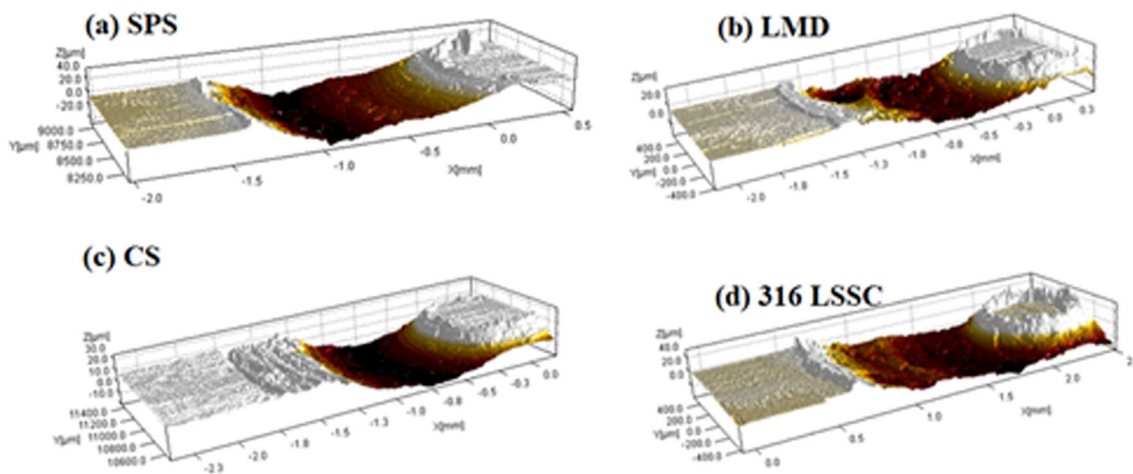

Fig. 8 Wear track of differently processed samples after the high-temperature tribotests. (a) SPS, (b) LMD, (c) CS, and (d) 316 LSSC

The value of friction at high temperature is decided by a number of factors such as thermal expansion, surface oxidation, and lubricants (Ref 36). In general, materials can get soften and expand and hence can result in increase in friction. However, 316 SS is well known for its high-temperature strength and low thermal expansion. This may be the reason for the nearly same average COF for SPS, LMD, and CS samples. Reduction of friction in commercial grade sample can be attributed to the relatively lower hardness and higher oxidation/thermal expansion compared to the other samples.

As compared to the ambient test, high-temperature test caused in a significant reduction in the fluctuation of the COF values. Even though the average COF is a piece of useful information, the instantaneous value of COF and stability of force have to be considered while selecting a material for engineering applications such as machine design and optimization. Lower fluctuation also points to a steady wear rate. Hence, the high-temperature tested samples (except SPS case) have steadier wear rate as compared to the room temperature test. The time-varying frictional values of each samples depend on many factors such as local melting due to high temperature, oxidation process, debris trapped between the sample and

counter body, and contact and non-contact nature of the materials surface due to the difference on surface roughness.

(ii) Wear

The contact area of the ball increases with increasing sliding distance. The wear track at the end of the high-temperature tribotests is shown in Fig. 8. The 3D profile of the track shows that the cold sprayed sample has undergone minimum wear compared to other samples. A visual inspection reveals that SPS and 316 LSSC samples have similar track widths, however, higher compared to that of LMD. The track depth for all samples was smaller for HT tribo-tested samples (500 °C) compared to the corresponding room temperature values. To calculate the wear volume and wear rate of each samples, two-dimensional depth profiles were recorded as shown in Fig. 9(a). The calculated wear rate of all samples is plotted in Fig. 9(b).

The 2D profiles in Fig. 9(a) show a zig–zag wear contour as compared to the corresponding room temperature profiles. The wear volume observed at 500 °C for SPS, LMD, CS, and 316 LSSC are 0.281, 0.155, 0.113, and 0.33 mm^3, respectively. The
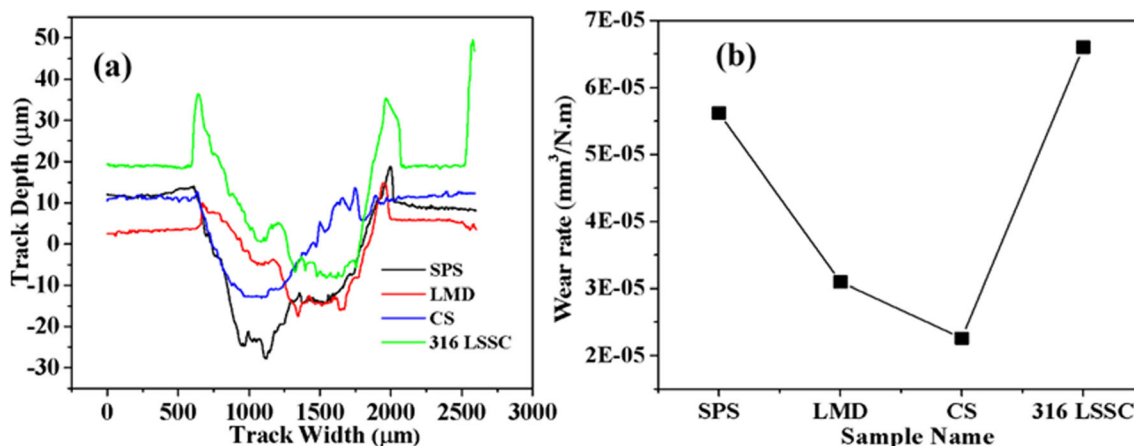
Fig. 9 (a) Wear track depth vs. width profile and (b) wear volume calculated from the depth profiles
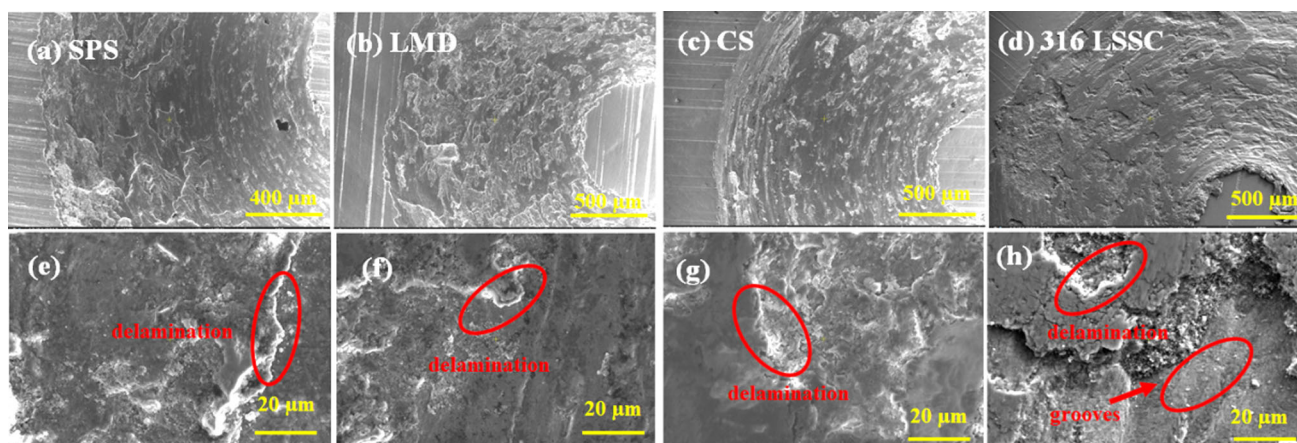

Fig. 10 (a-d) FESEM images of the high-temperature wear tracks with (e-g) the equivalent magnified version of the tracks

cold spray sample has the lowest wear rate (2.1×10^{-5} mm^3/N m) at high temperature, though the equivalent value at room temperature showed the highest among all. An 84% reduction in wear rate was observed for CS sample while the LMD sample showed a reduction of 54% as compared to their room temperature values. The CS sample used for the tribotest was as-sprayed one without any post-annealing process. Hence, the enhancement in wear resistance could be attributed to annealing-induced structural changes during the high-temperature tribotest. Many processes such as grain growth and recrystallization can take place during annealing depending on the annealing temperature and duration. Li et al. (Ref 33) showed that annealing of cold sprayed Cu coating resulted in a notable microstructural evolution. They observed that the elongated particles turned back to their feedstock size. The weakly bonded particles strengthen the bond during annealing through surface diffusion similar to solid-state diffusion-based bonding process (Ref 37).

Further, it was reported that microstructural fatigue cracks get healed during the annealing process (Ref 38). This means that the interfacial bonding area between two particles increased with increase in the annealing time. For the SPS and commercial grade samples, observed wear rate values are slightly higher than the equivalent room temperature values. In these samples, high temperature might have affected the

strength and hardness of the material which caused increased wear rate. However, LMD showed a reduction in the wear rate at high temperature. This may be possibly due to the increase in material hardness, decrease in thermal stress.

The FESEM images of the wear tracks (Fig. 10) were recorded to understand the wear mechanism at high temperatures. Abrasive wear and adhesive wear are the major wear mechanisms in all the samples during the tribotest. A small amount of adhesive wear was found to exist as we could see (the zirconia ball had a slightly blackish shade after the test) a little material transfer from the pellet to the zirconia ball. Abrasion in general takes place due to the roughness and hardness difference between the mating surfaces. The delamination in which the material fractures into layers is evidenced from the SEM images shown in Fig. 10(e and f). The severity of the wear varied from sample to sample depending on the material bonding, density, hardness, and yield strength. A high heating rate of ~ 30 °C/min could also have significantly influenced the wear rate.

The EDS analysis on the wear tracks was carried out to understand the oxidation and material transfer from the zirconia ball to the pellet during the high-temperature tribotest. The elemental composition obtained from the EDS spectra is tabulated in Table 2. The oxygen and zirconium content were found to be maximum in the cold spray sample. The oxide layer

formation in the cold spray sample might have acted as a barrier layer to prevent the direct contact between the body and counter body. A slightly higher amount of zirconia content compared to other samples may be due to the higher hardness of the cold spray sample compared to the other samples. The presence of zirconia in all the samples shows the wear of the counter body. The EDS spectrum corresponding to each sample, and the SEM images of the analyzed area are shown in Fig. S1 and Fig. S2, respectively.

When zirconia and steel are in contact, the wear behavior will depend on the relative hardness of the materials and the operating conditions. In the present case, as the zirconia is harder, it was not undergone much wear, as it is also evident from the visual appearance of the Zr ball used. In general, zirconia is harder than steel, which means that it can cause more wear on the steel surface. By using lubricant and optimizing the operating conditions, wear between zirconia and steel can be reduced. Table 2 of the manuscript basically shows the elemental composition (in wt.%) of differently processed samples. The wt.% of zirconia present in different samples varies from 5 to 15 wt.%. This shows the wear on counter body.

3.3 Erosion Studies

A solid particle erosion test was carried out to evaluate the performance of 316 stainless steels and the effect of different processing routes on the erosion rate. The sand blaster set up used for the studies is shown in Fig. 11(a). The morphology of the alumina (Al_2O_3) particles which are used as erodent is shown in Fig. 11(b). Average particle size of Al_2O_3 particle (natural alumina 97% purity) is 150 μm. A sand particle flux of 65 kg/m^2/s corresponding to a sand flow rate of 4 g per second is used for the erosion tests at different impinging angles. The

Table 2 The elemental composition (in wt.%) of differently processed samples

Elements	SPS	LMD	CS	316 LSSC
O K	8.5 ± 0.5	12.7 ± 0.5	13.2 ± 0.5	10.6 ± 0.5
Ni L	8.1 ± 0.5	7.3 ± 0.5	6.7 ± 0.5	1.6 ± 0.05
Zr L	6.4 ± 0.5	8.8 ± 0.5	14.9 ± 0.5	5.0 ± 0.5
Mo L	1.0 ± 0.01	0.7 ± 0.1	0.5 ± 0.05	0.9 ± 0.1
Cr K	16.3 ± 0.5	14.4 ± 0.5	12.9 ± 0.5	17.5 ± 0.5
Fe K	59.7 ± 0.5	56.2 ± 0.5	51.9 ± 0.5	64.4 ± 0.5

samples before and after the test were cleaned with acetone and dried using a drier and weighed using a weighing balance to calculate the weight loss (ΔW). The erosion rate (E_r) in these studies is calculated using the following equation:

$$E_r = \frac{\Delta W}{W_s} = \frac{(W_{final} - W_{initial})}{W_s} \qquad \text{(Eq 1)}$$

where W_s is the weight of the sand consumed during the test, and $W_{initial}$ and W_{final} are the weight of the sample before and after the test, respectively.

In addition to the weight loss calculation, the surface profiles of all the substrates after the erosion test were analyzed to understand the crater depth details using surface profilometer, and the 3D images for the two impinging angles are shown in Fig. 12. For the 90° impinging angle, the cold sprayed sample was found to give more crater depth and width while the commercial grade showed minimum. The circular/spherical scars slowly change to elliptical ones when the impinging angle changed from 90° to 45°. The erosion was observed to be more for the 45° impinging angle as compared to that of 90° case. The LMD sample showed similar performance to that of commercial steel. However, the erosion of SPS sample lies between LMD and commercial grade. The erosion rate is found to be a function of the blasting angle. The lower erosion rate at a higher impinging angle can be attributed to higher particle–particle interaction. For higher impinging angles, erodent particles bounced back from the substrate surface can interact with the incoming particles and result in a large number of collisions between the incident and rebounded particles. Hence, a larger number of the incident particles get deflected from their incident trajectory and pushed away from the center of the substrates (Ref 16). At oblique incident angles on ductile materials, higher erosion rate and significant deformation can be attributed to the cutting and plowing actions. These are the reasons for the observed difference in the erosion between lower and higher impinging angles.

Two-dimensional depth profiles obtained from the 3D scans for both the angles are shown in Fig. 13(a) and (b). Among all substrates, the cold spray sample showed the highest crater depth of 252 and 268 μm, respectively, at impinging angle of 90° and 45°. The commercial and LMD samples showed nearly the same erosion depth at both the angles. The SPS sample has a slightly higher erosion depth as compared to LMD, however, lower value when compared to cold spray sample. Variation in scar depth values for various samples is plotted in Fig. 14(a).
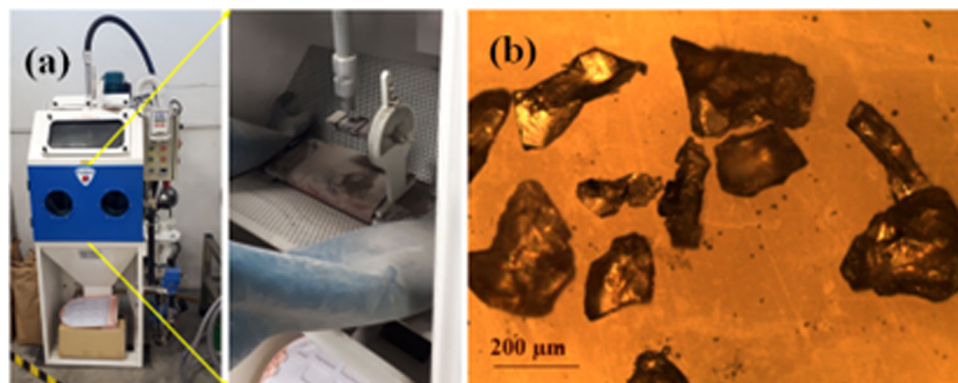

Fig. 11 (a) Sand blaster apparatus used for the erosion studies with a magnified version of sample chamber with sample holder and the blast nozzle, and (b) optical image showing the morphology of the erodent particles
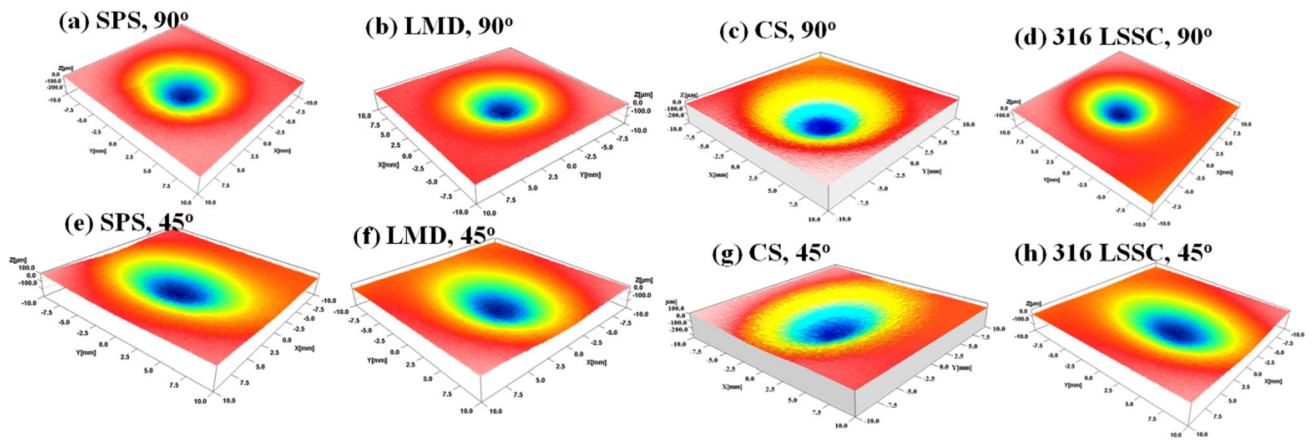
Fig. 12 Three-dimensional images of the eroded substrates of differently processed steels at two blasting angles, *viz*, 90° and 45°
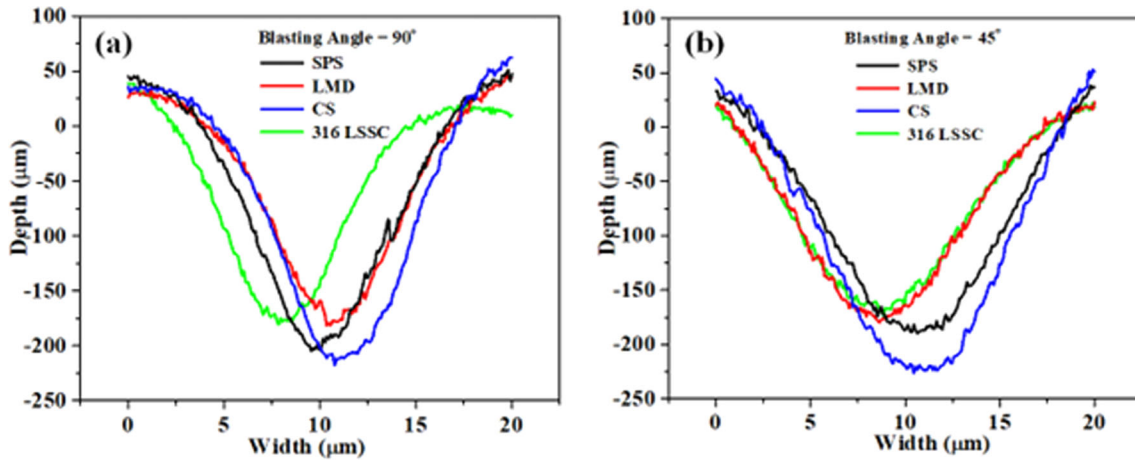

Fig. 13 Erosion depth vs. width of the erosion scars of all the samples for a blasting angle of (a) 90° and (b) 45°
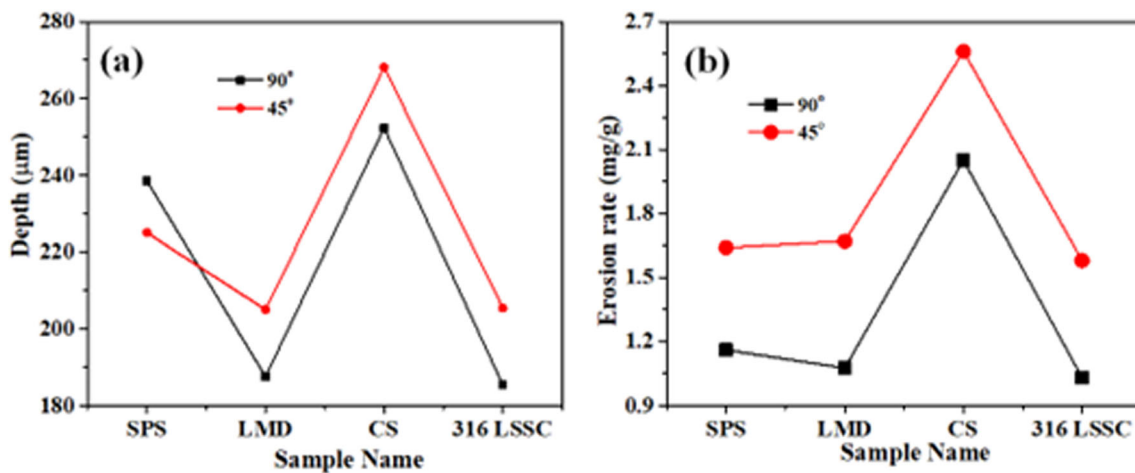

Fig. 14 (a) Erosion depth and (b) erosion rate at blasting angle of 90° and 45° for the differently processed samples

The cold spray sample showed the lowest erosion resistance due to weaker particle–particle bonding in the as-sprayed material matrix. An increase in resistance to erosion was observed if the sample was post-annealed after cold spraying (Ref 39–41). This may be attributed to the fact that the post-annealing can enhance the interparticle strength. In the present paper, such a post-annealing process has not been performed. High-temperature (∼ 1500 °C) processing of the commercial

Table 3 Table summarizes the wear and erosion rates of the samples under various experimental conditions

Process method	Process temperature, °C	Wear rate, $10^{-4} \times mm^3/N$ m	Erosion rate, mg/g
Laser melt deposition	~ 1500 °C	0.7@RT	1.67@45°
		0.3@500 °C	1.07@90°
Spark plasma sintering	~ 1000 °C	0.4@RT	1.64@45°
		0.6@500 °C	1.16@90°
Cold spray	~ 400 °C (gas heating temperature)	1.4@RT	2.56@45°
		0.2@500 °C	2.05@90°

grade sample imparted high bond strength between the particles and resulted in higher erosion resistance. In the laser-based additive manufacturing methods, bonds among the particles are stronger as in the case of commercial graded steel due to high process temperature. For the SPS sample, the lower sintering temperature of ~ 1000 °C caused lower erosion resistance as compared to LMD and casted samples.

Erosion rate is calculated using the Eq. 1 and plotted in Fig. 14(b) for different samples at two blasting angles. The erosion rate is highest for the cold spray sample while the commercial graded sample showed a minimum at 90° and 45° impinging angles. The highest erosion rate in the CS sample (~ 2 mg/g) might be due to the comparatively weaker bonding between the as-sprayed particles. LMD and SPS samples are as good as commercially prepared steel in terms of erosion. The erosion mechanisms, such as indenting, cutting, sliding, or plowing, are a function of the impact angle (Ref 16) and, hence, the observed difference in erosion rate. The erosional rate determines the application of a given material for erosion-related application. For example, LMD gives an erosion rate of 1 mg/g at 90°. This implies that structures with arbitrary shape and size can be easily prepared by LMD and hence useful for many specific applications in an erosive environment. The higher erosion rate in the cold sprayed sample needs to be addressed either by post-annealing or surface coating with harder material.

Finally, we have compared our work with some of the similar kinds of work (Ref 12, 42–45) and shown in Table S1. In summary, the present work gives a glimpse in finding the suitable process so as to get the desired wear and erosion behavior. As additive manufacturing method is a way forward to make many complex shapes and sizes, information about the properties of LMD and cold sprayed samples is important for tuning the material properties of steel and other alloys. The cold spray sample had the highest wear volume and erosion rate at room temperature tribo- and erosion tests. However, at the high-temperature tribotest, the cold sprayed sample displayed the lowest wear resistance compared to other samples. It is rare to see the comparative studies of the influence of the process methods on the material properties, and in this way, this paper gives new directions. In each process, a lot of optimization could be done to enhance the wear and resistance to erosion. This work can further be extended to many directions such as comparison of processes for materials other than steel, post-annealing effect of cold sprayed samples, influence of sintering temperature on the properties of SPS processed samples, etc. High-temperature erosion tests can reveal the usefulness of a material for high-temperature applications. Erosion test can be done at different impinging angles, various sand flow rates, and different erodent particles. The erosion scar analysis by HRSEM helps in understanding the erosion mechanism.

Even though there are many recent reports on the tribological properties of various AISI graded steels (Ref 46–49), the present study focused mainly on the wear and erosion rate of AISI 316 LSS processed by different methods. The essential results obtained from the present study are shown in Table 3. As shown, for the room temperature (RT) applications, spark plasma sintered (SPS) pellets gave best erosion (at 45° impact angle) and wear rate compared to other samples; when it comes to high-temperature (HT) applications, laser melt deposition (LMD) is the best suited method (at 90° impact angle). Overall, the performance of LMD samples is quite promising at different wear testing temperatures and erosion impact angles.

4. Conclusions

This study explores the impact of fabrication methods on the tribology and erosion resistance behavior of 316L SS. Tribo- and erosion tests conducted at room temperature revealed that the cold sprayed sample is more susceptible to wear, and erosion compared to other samples. This might be due to the comparatively weaker bonding between the as-sprayed particles. However, the cold sprayed sample showed the highest wear resistance during tribotests at 500 °C. This suggests that post-annealing of the as-sprayed sample enhances the interparticle bond strength. The commercial grade and SPS samples have nearly the same wear resistance while the LMD sample showed a slightly lower wear resistance during room temperature tribotest. Wear resistance was reduced for all samples at 500 °C except for the cold sprayed sample which might be due to the microstructural changes at 500 °C. The values of wear volume, coefficient of friction, and erosion rate at various experimental conditions reveal the performance and lifetime of 316L SS for different applications. LMD is promising in making any complex structures, and in case of 316L SS, it imparts good erosion resistance and wear resistance at room temperature. The cold sprayed sample has potential to repair damaged components as well as making new components. However, the as-sprayed material properties need to be further modified to suit low-temperature wear and erosive applications. Optimization of the process parameters is as important as the selection of a specific process for material fabrication. More research in this area is, therefore, warranted.

Conflict of interest

The authors declare no potential conflicts of interest with respect to the research, authorship, and publication of this article.

References

1. A.V. Radhamani, H.C. Lau, and S. Ramakrishna, CNT-Reinforced Metal and Steel Nanocomposites: A Comprehensive Assessment of Progress and Future Directions, *Compos. A Appl. Sci. Manuf.*, 2018, **114**, p 170–187
2. A.V. Radhamani et al., Structural, Mechanical and Tribological Investigations of CNT-316 Stainless Steel Nanocomposites Processed via Spark Plasma Sintering, *Tribol. Int.*, 2020, **152**, 106524
3. T.D. Ngo et al., Additive Manufacturing (3D printing): A Review of Materials, Methods, Applications and Challenges, *Compos. B Eng.*, 2018, **143**, p 172–196
4. V. Mamedov, Spark Plasma Sintering as Advanced PM Sintering Method, *Powder Metall.*, 2002, **45**, p 322–328
5. A. Gasser et al., Laser Additive Manufacturing, *Laser Tech. J.*, 2010, **7**(2), p 58–63
6. A. Moridi et al., Cold Spray Coating: Review of Material Systems and Future Perspectives, *Surf. Eng.*, 2014, **30**(6), p 369–395
7. M. Ma, Z. Wang, and X. Zeng, A Comparison on Metallurgical Behaviors of 316L Stainless Steel by Selective Laser Melting and Laser Cladding Deposition, *Mater. Sci. Eng., A*, 2017, **685**, p 265–273
8. G.M.E. Cooke, An Introduction to the Mechanical Properties of Structural Steel at Elevated Temperatures, *Fire Saf. J.*, 1988, **13**(1), p 45–54
9. I.-R. Choi, K.-S. Chung, and H. Lee, Thermal and Mechanical Properties of Structural Steel SN400 at Elevated Temperatures, *Int. J. Steel Struct.*, 2017, **17**(3), p 999–1007
10. M. Ziętala et al., The Microstructure, Mechanical Properties and Corrosion Resistance of 316L Stainless steel Fabricated Using Laser Engineered Net Shaping, *Mater. Sci. Eng., A*, 2016, **677**, p 1–10
11. I. Tolosa et al., Study of Mechanical Properties of AISI 316 Stainless Steel Processed by "Selective Laser Melting", Following Different Manufacturing Strategies, *Int. J. Adv. Manuf. Technology*, 2010, **51**(5), p 639–647
12. S. Alvi, K. Saeidi, and F. Akhtar, High Temperature Tribology and Wear of Selective Laser Melted (SLM) 316L Stainless Steel, *Wear*, 2020, **448–449**, 203228
13. F. Bartolomeu et al., 316L Stainless Steel Mechanical and Tribological Behavior—A Comparison Between Selective Laser Melting, Hot Pressing and Conventional Casting, *Addit. Manuf.*, 2017, **16**, p 81–89
14. Y. Sun, A. Moroz, and K. Alrbaey, Sliding Wear Characteristics and Corrosion Behaviour of Selective Laser Melted 316L Stainless Steel, *J. Mater. Eng. Perform.*, 2013, **23**(2), p 518–526
15. Zhu, Y., et al., *Tribology of selective laser melting processed parts: Stainless steel 316 L under lubricated conditions.* Wear, 2016. p. 350-351
16. V.B. Nguyen et al., Effect of Air-Borne Particle–Particle Interaction on Materials Erosion, *Wear*, 2015, **322–323**, p 17–31
17. P.H. Shipway, The Effect of Plume Divergence on the Spatial Distribution and Magnitude of Wear in Gas-Blast Erosion, *Wear*, 1997, **205**(1), p 169–177
18. M. Liebhard and A. Levy, The Effect of Erodent Particle Characteristics on the Erosion of Metals, *Wear*, 1991, **151**(2), p 381–390
19. V.B. Nguyen et al., Effect of Particle Size on Erosion Characteristics, *Wear*, 2016, **348–349**, p 126–137
20. A.A. Gadhikar et al., Effect of Carbides on Erosion Resistance of 23-8-N Steel, *Bull. Mater. Sci.*, 2014, **37**(2), p 315–319
21. R.J.K. Wood et al., Influence of Microstructure on the Erosion and Erosion–Corrosion Characteristics of 316 Stainless Steel, *Wear*, 2013, **306**(1–2), p 254–262
22. J.R. Laguna-Camacho et al., Solid Particle Erosion of AISI 304, 316 and 420 Stainless Steels, *Wear*, 2013, **301**(1–2), p 398–405
23. A.A.C. Recco, D. López, A.F. Bevilacqua, F. da Silva, and A.P. Tschiptschin, Improvement of the Slurry Erosion Resistance of an Austenitic Stainless Steel With Combinations of Surface Treatments: Nitriding and TiN Coating, *Surface and coatings Technology*, 2007, **202**(4–7), p 993–997
24. L. Łatkaa, M. Szalab, M. Michalaka, and T. Pałkac, Impact of Atmospheric Plasma Spray Parameters on Cavitation Erosion Resistance of Al2O3–13% TiO2 Coatings, *Acta Phys. Pol., A*, 2019, **136**, p 342–347
25. L. Łatka, M. Michalak, M. Szala, M. Walczak, P. Sokołowski, and A. Ambroziak, Influence of 13 wt% TiO2 Content in Alumina-Titania Powders on Microstructure, Sliding Wear and Cavitation Erosion Resistance of APS Sprayed Coatings, *J. Surf. Coat. Technol.*, 2021, **410**, 126979
26. A.V. Radhamani, H.C. Lau, and S. Ramakrishna, 316L Stainless Steel Microstructural, Mechanical, and Corrosion Behavior: A Comparison Between Spark Plasma Sintering, Laser Metal Deposition, and Cold Spray, *J. Mater. Eng. Performance*, 2021, **30**, p 3492–3501
27. N. Hansen, Hall-Petch Relation and Boundary Strengthening, *Scripta Mater.*, 2004, **51**(8), p 801–806
28. M.A. Meyers, K.P. Staudhammer, and L.E. Murr Eds., *Metallurgical Applications of Shock-Wave and High-Strain-Rate Phenomena*, Marcel Dekker Inc, New York, 1986, p 451
29. H. Conrad, Grain Size Dependence of the Plastic Deformation Kinetics in Cu, *Mater. Sci. Eng., A*, 2003, **341**(1), p 216–228
30. A.J.W. Moore and W.M. Tegart, Relation Between Friction and Hardness, *Proc. R. Soc. Lond. Ser. Math. Phys. Sci.*, 1952, **212**(1111), p 452–458
31. M.O.A. Mokhtar, The Effect of Hardness on the Frictional Behaviour of Metals, *Wear*, 1982, **78**(3), p 297–304
32. P. J, Blau, *Four great challenges confronting our understanding and modeling of sliding friction.* Amsterdam: Elsevier, Tribology for Energy Conservation, Volume 34, 1st Edition, 1998: p. 177–228
33. W.-Y. Li, C.-J. Li, and H. Liao, Effect of Annealing Treatment on the Microstructure and Properties of Cold-Sprayed Cu Coating, *J. Therm. Spray Technol.*, 2006, **15**(2), p 206–211
34. A. Papyrin, *Cold Spray Technology*, Elsevier, Oxford, 2007
35. R.C. McCune et al., Characterization of Copper Layers Produced by Cold Gas-Dynamic Spraying, *J. Therm. Spray Technol.*, 2000, **9**(1), p 73–82
36. S.R. Pearson, P.H. Shipway, J.O. Abere, and R.A.A. Hewitt, The Effect of Temperature on Wear and Friction of a High Strength Steel in Fretting, *Wear*, 2013, **303**(1–2), p 622–631
37. V.M. Falchenko, *Diffusion Processes in Solid-Phase Welding of Materials*, Oxonian Press, New Delhi, 1984
38. H.L. Zhang et al., Morphological Healing Evolution of Penny-Shaped Fatigue Microcracks in Pure Iron at Elevated Temperatures, *Appl. Phys. Lett.*, 2004, **85**(7), p 1143–1145
39. W. Sun, A.W.Y. Tan, K. Wu, S. Yin, X. Yang, I. Marinescu, and E. Liu, Post-Process Treatments on Supersonic Cold Sprayed Coatings: A Review, *Coatings*, 2020, **10**(2), p 123
40. X. Xie, C. Chen, Z. Chen, A. Addad, Y. Xie, H. Wu, and H. Liao, Effect of Annealing Treatment on Microstructure and Mechanical Properties of Cold Sprayed TiB2/AlSi10Mg Composites, *Surf. Interfaces*, 2021, **26**, p 101341
41. M. Kazasidis, E. Verna, S. Yin, and R. Lupoi, The Effect of Heat Treatment and Impact Angle on the Erosion Behavior of Nickel-Tungsten Carbide Cold Spray Coating Using Response Surface Methodology, *Emerg. Mater.*, 2021, **4**(6), p 1605–1618
42. W.-S. Shin, B. Son, W. Song, H. Sohn, H. Jang, Y.-J. Kim, and C. Park, Heat Treatment Effect on the Microstructure, Mechanical Properties, and Wear Behaviors of Stainless steel 316L Prepared via Selective Laser Melting, *Mater. Sci. Eng., A*, 2021, **806**, 140805
43. J.R. Laguna Camacho, A. Marquina Chavez, J.V. Mendez Mendez, M. Vite-Torres, and E.A. Gallardo Hernandez, Solid Particle Erosion of AISI 304,316 and 420 Stainless Steels, *Wear*, 2013, **301**, p 398–405
44. R.J.K. Wood, J.C. Walker, T.J. Harvey, S. Wang, and S.S. Rajahram, Influence of Microstructure on the Erosion and Erosion–Corrosion Characteristics of 316 Stainless Steel, *Wear*, 2013, **306**, p 254–262
45. H. Meng, X. Hu, and A. Neville, A Systematic Erosion–Corrosion Study of Two Stainless Steels in Marine Conditions via Experimental Design, *Wear*, 2007, **263**, p 355–362
46. C. Carboga, B. Aktas, and B. Kurt, Dry Sliding Wear Behavior of Boron-Doped 205 Manganese Steels, *J. Mater. Eng. Performance*, 2020, **29**, p 3120–3126

47. B. Aktaş, M. Toprak, A. Çalık, and A. Tekgüler, Effect of Pack-Boriding on the Tribological Behavior of Hardox 450 and HiTuf Steels, *Rev. Adv. Mater. Sci.*, 2020, **59**(1), p 314–321

48. S. Dabas and P. Kumar, A Review on Tribological Behaviour of Steel Against Steel, *Mater. Today Proc.*, 2021, **44**, p 4822–4826

49. N. Angsuseranee, B. Watcharasresomroeng, P. Bunyawanichkul, S Chartniyom, Tribological Behavior of Tool Steel Substrate and Solid Films against 304 BA Austenitic Stainless Steel under Dry Sliding, Hindawi, *Adv. Tribol, 2020. Article ID 8845548*